12.3 **GROWTH OF CLOUD DROPLETS BY TURBULENT COLLISION-COALESCENCE**

Yan Xue[1], Lian-Ping Wang[1]*, and Wojciech W. Grabowski[2]

[1] Department of Mechanical Engineering, University of Delaware, Newark, Delaware 19716-3140, USA

[2] Mesoscale and Microscale Meteorology Division, National Center for Atmospheric Research
PO Box 3000, Boulder, Colorado 80307-3000, USA

Abstract

An open question in warm rain process and precipitation formation is how rain forms in warm cumulus as rapidly as it has sometimes been observed. In general, the rapid growth of cloud droplets across the size gap from 10 to 50 μm in radius has not been fully explained. In this paper, we focus on the growth of cloud droplets by collision-coalescence taking into account both the gravitational mechanism and various enhancements of the collision-coalescence rate due to airflow turbulence. Based on recent direct simulation results of collection rates of settling droplets in atmospheric turbulence, several effects of airflow turbulence on the collection kernel are considered, including (1) the enhanced relative motion due to differential acceleration and shear effects, and (2) enhanced average pair density due to local clustering of droplets. The kinetic collection equation (KCE) is solved with an accurate bin-integral method and newly developed parameterizations of turbulent collection kernels. The bin-integral method allows for a precise study of the collision-coalescence growth in terms of any initial size distribution and a prescribed form of the collection kernel.

Based on recent results from direct simulations and theoretical modeling, we utilize four different turbulent collection kernels to study the time evolution of droplet size distribution. The results are compared with the base case using the hydrodynamical-gravitational collection kernel of Hall (1980). Under the conditions typical of atmospheric clouds, it is found that air turbulence has a measurable impact on both the collection kernel and the time interval for the formation of drizzle drops. For the best available, turbulent geometrical kernel, we find that the air turbulence can shorten the time for the formation of drizzle drops by about 40% relative to the base case, in terms of both radar reflectivity and the mass-weighted size. A methodology is also developed to unambiguously identify the three phases of droplet growth, namely, the autoconversion phase, the accretion phase, and the larger hydrometeor self-collection phase. The important observation is that a moderate enhancement of collection kernel by turbulence can have a significant impact on the autoconversion phase of the growth. Should the enhancement of collision efficiency by turbulence be included, the airflow turbulence could easily shorten the time for the formation of drizzle drops by a factor of two.

*Corresponding author's address: Lian-Ping Wang, Department of Mechanical Engineering, 126 Spencer Laboratory, University of Delaware, Newark, Delaware 19716-3140, USA. E-mail: lwang@me.udel.edu

1. INTRODUCTION

The growth of cloud droplets by collision-coalescence is a key step in the formation of warm rain (Pruppacher and Klett 1997). The rate of collisions is controlled by both the gravitational mechanism and various effects of air turbulence. The rate of collision-coalescence is usually quantified through the collection kernel.

The objective of this paper is to provide some preliminary understanding of how the effects of air turbulence on the geometric collision kernel alter the size evolution of cloud droplets. This in part is motivated by the recent study of Riemer and Wexler (2005) who solved the kinetic collection equation (KCE) using the turbulent collision kernel of Zhou *et al.* (2001) (hereafter will be referred to as the ZWW-RW kernel). Wang *et al.* (2006a) pointed out several drawbacks and limitations of the ZWW-RW kernel, which questioned the relevance of the conclusions of Riemer and Wexler (2005) to the growth of cloud droplets. Here we shall consider several improved versions of turbulent collision kernels relevant to cloud droplets. We will compare the magnitudes of different kernels and investigate their resulting size distributions starting from an identical initial size distribution.

2. TURBULENT COAGULATION PROCESS

Over the last 10 years, quite a few studies have been published in both engineering and atmospheric literature concerning the collision rate of particles in a turbulent flow, see discussions in Jonas (1996), Pinsky and Khain (1997), Vaillancourt and Yau (2000), Shaw (2003), Wang *et al.* (2005b), Ayala (2005). These studies suggest, at least qualitatively, that the enhancement of the collision-coalescence mechanism associated with the cloud turbulence might be a likely explanation for the rapid growth of cloud droplets across the size gap from roughly 10 μm to about 60 μm in radius. Our improved understanding of the role of air turbulence is based mostly on numerical simulations and qualitative theoretical arguments. It has been shown that the collision rate of cloud droplets can be enhanced by several effects of turbulence, including (1) enhanced relative motion due to differential acceleration and shear effects, (2) enhanced average pair density due to local preferential concentration of droplets, (3) enhancement due to selective alterations of the settling rate by turbulence, and (4) enhanced collision efficiency. The first three effects are related to the geometric collision kernel $\Gamma^g(x, y)$, and the last effect is quantified in terms of the collision efficiency $E(x, y)$. Assuming that the coalescence efficiency is close to unity, the collection kernel is the product of $\Gamma^g(x, y)$ and $E(x, y)$. Further details of the kinematic formulation of the collection kernel are given in Wang *et al.* (2005b).

The levels of enhancement of the collection kernel by air turbulence depend, in a complex manner, on the size of droplets (which in turn determines the response time and settling velocity) and the strength of air turbulence (i.e., the dissipation rate, Reynolds number, *etc.*). In a recent study, Ayala (2005) developed an analytical model for the geometric collision rates of cloud droplets. This is a step forward than the previous models of Zhou *et al.* (2001) and Wang *et al.* (2000) who considered only non-settling particles.

3. TURBULENT COLLISION KERNELS

In this section, we introduce several formulations of turbulent collision kernel and discuss how the relevant physical mechanisms are included in these kernels. The Hall kernel (Hall 1980) will be used as a base case to compare the relative impact of air turbulence. The Hall kernel is a hydrodynamical gravitational kernel without effects of air turbulence. This is a popular kernel often used by the cloud physics community to study the growth of cloud droplets by collision-coalescence.

3..1 The ZWW-RW kernel

This first turbulent collision kernel is a kernel developed by Zhou *et al.* (2001) (ZWW01 in short) and was used by Riemer and Wexler (2005) (RW05 in short) to study the growth of cloud droplets by turbulent collision-coalescence. The Stokes drag law was assumed and the gravitational settling was not considered in ZWW01. In RW05, the gravitational effect was treated separately by adding the Hall kernel to the parameterization of Zhou *et al.* (2001). The details of the ZWW-RW kernel are as follows.

In ZWW01, the turbulent geometric collision kernel in a bidisperse system was considered. It included the effect of turbulence on the relative velocity between two colliding droplets (the transport effect) and the non-uniform droplet distribution due to the interaction between particles and their surrounding airflow vortical structures (the accumulation effect). No consideration was given to the gravitational settling.

Their model is based on the general kinematic formulation (*e.g.*, Wang *et al.* 2005b) of the geometric collision kernel in the form of

$$\Gamma_{ij}^g = 2\pi R^2 < |w_r|(r = R) > g_{ij}(r = R), \qquad (1)$$

Here, the geometric collision radius R is defined as $R = r_i + r_j$. w_r is the radial relative velocity between a particle from size group i and size group j. The average radial relative velocity $\langle |w_r| \rangle$ describes the turbulent transport effect. ZWW01 represented $\langle |w_r| \rangle$ as

$$\langle |w_r| \rangle = \left[\frac{2}{\pi} (\langle w_{r,accel}^2 \rangle + \langle w_{r,shear}^2 \rangle) \right]^{1/2}, \qquad (2)$$

where $\langle w_{r,accel}^2 \rangle$ represents the contribution due to differential fluid acceleration, and $\langle w_{r,shear}^2 \rangle$ is the contribution due to local fluid shear (e.g., Saffman and Turner 1956). According to Wang *et al.* (2000) and ZWW01, $\langle w_{r,shear}^2 \rangle$ and $\langle w_{r,accel}^2 \rangle$ can be obtained by

$$\langle w_{r,shear}^2 \rangle = \frac{1}{15} {v_k}^2 \left(\frac{R}{\eta} \right)^2, \qquad (3)$$

and

$$\langle w_{r,accel}^2 \rangle = C_w(z) \langle w_{accel,0}^2 \rangle, \qquad (4)$$

respectively. $C_w(z)$ is given as

$$C_w(z) = 1.0 + 0.6 \exp[-(z - 1)^{1.5}]. \qquad (5)$$

Here, z = max$(\theta_i/\theta_j,\ \theta_j/\theta_i)$. θ_i is defined as $\theta_i = 2.5\tau_{pi}/T_L$. τ_{pi} is the cloud droplet inertial response time with the form $\frac{2\rho_w r_i^2}{9\nu\rho_a}$. ρ_w is the water density set to 1000 kg/m^3. ρ_a is the density of air and equal to 1.225 kg/m^3 in our code. ν is the dynamic viscosity of air with the value 1.818×10^{-4} m^2/s in our code. T_L is the flow integral time scale and is equal to u'^2/ϵ. u' is the fluctuation turbulent flow velocity and ϵ is the dissipation rate of turbulent flow. For heavy particles ($\rho_w/\rho_a \gg 1$), $< w_{accel,0}^2 >$ can be calculated as

$$\begin{aligned} \langle w_{accel,0}^2 \rangle \quad &= \quad \frac{u'^2 \gamma}{\gamma - 1} \\ &\times \left\{ (\theta_i + \theta_j) - \frac{4\theta_i\theta_j}{\theta_i + \theta_j} \left[\frac{1 + \theta_i + \theta_j}{(1 + \theta_i)(1 + \theta_j)} \right]^{1/2} \right\} \\ &\times \left[\frac{1}{(1 + \theta_i)(1 + \theta_j)} - \frac{1}{(1 + \gamma\theta_i)(1 + \gamma\theta_j)} \right]. \qquad (6) \end{aligned}$$

Here, γ is a function of z:

$$\gamma = z \times 0.183 \frac{u'^2}{(\epsilon\nu)^{1/2}}. \qquad (7)$$

The radial distribution function $g_{ij}(R)$ $(i \neq j)$ measures the accumulation effect and is modeled as

$$g_{ij}(R) = 1.0 + \rho_{ij}\{[g_{ii}(R)-1][g_{jj}(R)-1]\}^{1/2}, \quad (8)$$

where the monodisperse radial distribution function $g_{kk}(R)$ $(k = i, j)$ parameterized as

$$\begin{aligned} g_{kk}(R) &= 1 + y_0(St)[1 - z_0^2(St)] \\ &\quad + z_0^2(St) R_\lambda \{y_1(St)[1 - z_1(St)] \\ &\quad + y_2(St) z_1(St) + y_3(St) z_2(St)\}, \quad (9) \end{aligned}$$

where the Stokes number St is defined as $St \equiv \tau_{pi}/\tau_k$ and $\tau_k = \sqrt{\nu/\epsilon}$. The functions $y_i(St)$ and $z_i(St)$ are defined as: $y_0(St) = 18St^2$, $y_1(St) = 0.36 St^{2.5}\exp(-St^{2.5})$, $y_2(St) = 0.24\exp(-0.5St)$, $y_3(St) = 0.013\exp(-0.07St)$, $z_0(St) = \frac{1}{2}\left[1+\tanh\frac{St-0.5}{0.25}\right]$, $z_1(St) = \frac{1}{2}\left[1+\tanh\frac{St-1.25}{0.1}\right]$, and $z_2(St) = \frac{1}{2}\left[1+\tanh\frac{St-6.5}{2.5}\right]$. The Taylor microscale Reynolds number R_λ is equal to $\sqrt{\frac{15}{\epsilon\nu}}u'^2$. The correlation coefficient $\rho_{ij}(\phi)$ is given as

$$\begin{aligned} \rho_{ij}(\phi) &= 2.6\exp(-\phi) + 0.205\exp(-0.0206\phi) \\ &\quad \times \frac{1}{2}[1.0 + \tanh(\phi - 3)], \quad (10) \end{aligned}$$

where $\phi \equiv \tau_{pj}/\tau_{pi}$.

Riemer and Wexler (2005) adopted the above kernel for the turbulent contribution. They then added the Hall kernel to it to account for the gravitational contribution as follows:

$$\begin{aligned} K_{ij} &= 2\pi R^2 <|w_r|(r=R)> g_{ij}(r=R) E_i^t j \\ &\quad + \pi R^2 |v_{pi} - v_{pj}| E_i^s j. \quad (11) \end{aligned}$$

Here, the collision efficiency $E_i^t j$ for the turbulent part is set to one, but the collision efficiency $E_i^s j$ for the gravitational part is assumed to be the same that used in the Hall kernel (Hall 1980).

As pointed out recently by Wang *et al.* (2006a), there are a number of drawbacks in the above ZWW-RW kernel including (a) the r.m.s. fluctuation velocity of the air turbulence was overestimated by a factor of $\sqrt{3}$, (b) the radial distribution function was overestimated due to the neglect of sedimentation in ZWW01, and (c) several inconsistent treatments of the turbulent contribution as compared to the gravitational contribution, namely, the use of the Stokes drag and unity collision efficiency for the turbulent contribution.

3..2 Modified ZWW kernels

We shall next introduce a modified turbulent kernel based on ZWW01. The parameterization is the same as that presented in the previous section for the turbulent contribution, but two modifications are implemented. The first is to replace the Stokes response time by a much more realistic inertial response time based on a nonlinear drag (Wang *et al.* 2006a) that would result in the same terminal velocity used in the Hall kernel. As shown in Wang *et al.* (2006a), the terminal velocity used in the Hall kernel is consistent with the known nonlinear drag law for small particles. The second change is the use of the correct r.m.s. fluctuation velocity of air turbulence, $u' = 2.0\ m/s$, based on observations (see Wang *et al.* 2006a).

Two versions of the modified ZWW kernel will be considered here. The first version only considers the turbulent contribution with the above two modifications and neglects the gravitational effect. This kernel will be referred to as *the modified ZWW kernel without gravity* or mZWWa in short. The same collision efficiency in the Hall kernel is applied to the mZWWa kernel.

The second version includes the gravitational contribution by adding to the above mZWWa kernel the Hall kernel as follows:

$$\begin{aligned} K_{ij} &= 2\pi R^2 E_{ij}^s \times \\ &\left\{\frac{2}{\pi}\left[\left(< w_{r,accel}^2 > + < w_{r,shear}^2 >\right) g_{ij}^2(r=R)\right.\right. \\ &\left.\left. + \frac{\pi}{8}|\mathbf{g}|^2(\tau_{pi} - \tau_{pj})^2\right]\right\}^{1/2} \quad (12) \end{aligned}$$

The terminal velocity in the Hall kernel is used here to define the effective inertial response time. This second version will be called *the modified ZWW kernel with gravity* or mZWWb in short.

3..3 The Ayala kernel

Very recently, Ayala (2005) (Ayala05 in short) developed a kernel based on direct simulations of turbulent collisions of sedimentation droplets. His study of the geometric collision kernel considered simultaneously the effects of air turbulence and gravity. Ayala05 also considered the hydrodynamic interactions in a turbulent air, although the results on turbulent collision efficiency are somewhat limited due to the amount of computational times required in the hybrid DNS approach he used (e.g., Ayala *et al.* 2006). In our preliminary study here, we only consider the effects of turbulence on the geometric collision kernel. The same collision efficiency and terminal velocity in the Hall kernel shall be employed. The additional effect of air turbulence on collision efficiency will be left for future research.

Starting with the same general formulation, Eq. (1), Ayala05 expressed the averaged radial relative velocity $< |w_r| >$ as

$$< |w_r| > = \sqrt{\frac{2}{\pi}}\left[\sigma^2 + \frac{\pi}{8}(\tau_{pi} - \tau_{pj})^2 |\mathbf{g}|^2\right]^{1/2}, \quad (13)$$

where the turbulent contribution to the relative motion is given by

$$\begin{aligned} \sigma^2 &= < (v'^{(j)})^2 > + < (v'^{(i)})^2 > \\ &\quad -2 < (v'^{(j)} v'^{(i)}) >, \quad (14) \end{aligned}$$

with

$$<(v'^{(k)})^2> \;=\; \frac{u'^2}{\tau_{pk}}\left[b_1 d_1 \Psi(c_1 e_1) - b_1 d_2 \Psi(c_1, e_2)\right. \\ \left. -b_2 d_1 \Psi(c_2, e_1) + b_2 d_2 \Psi(c_2, e_2)\right], \quad (15)$$

and

$$<(v'^{(i)} v'^{(j)})> \;=\; \frac{u'^2 f(R)}{\tau_{pi}\tau_{pj}}\left[b_1 d_1 \Phi(c_1 e_1) - b_1 d_2 \Phi(c_1, e_2)\right. \\ \left. -b_2 d_1 \Phi(c_2, e_1) + b_2 d_2 \Phi(c_2, e_2)\right], \quad (16)$$

where b_1, b_2, c_1, c_2, d_1, d_2, e_1, and e_2 are defined as

$$b_1 = \frac{1+\sqrt{1-2z^2}}{2\sqrt{1-2z^2}},\; b_2 = \frac{1-\sqrt{1-2z^2}}{2\sqrt{1-2z^2}},$$

$$c_1 = \frac{(1+\sqrt{1-2z^2})T_L}{2},\; c_2 = \frac{(1-\sqrt{1-2z^2})T_L}{2},$$

$$d_1 = \frac{1+\sqrt{1-2\chi^2}}{2\sqrt{1-2\chi^2}},\; d_2 = \frac{1-\sqrt{1-2\chi^2}}{2\sqrt{1-2\chi^2}},$$

$$e_1 = \frac{(1+\sqrt{1-2\chi^2})L_e}{2},\; e_2 = \frac{(1-\sqrt{1-2\chi^2})L_e}{2},$$

respectively. Here, $z = \tau_k/T_L$ and $\chi = \sqrt{2}\lambda/L_e$. λ is Taylor microscale and equal to $u'\sqrt{\frac{15\nu}{\epsilon}}$. L_e is Eulerian integral length scale of turbulence and equal to $0.5u'^3/\epsilon$. The function $\Phi(\xi,\zeta)$, taking $v_{p_i} > v_{p_j}$, is given by

$$\Phi(\xi,\zeta) = \left\{\frac{1}{\left(\frac{v_{p_j}}{\zeta} - \frac{1}{\tau_{p_j}} - \frac{1}{\xi}\right)} - \frac{1}{\left(\frac{v_{p_i}}{\zeta} + \frac{1}{\tau_{p_i}} + \frac{1}{\xi}\right)}\right\}$$
$$\times \frac{v_{p_i} - v_{p_j}}{2\zeta\left(\frac{v_{p_i}-v_{p_j}}{\zeta} + \frac{1}{\tau_{p_i}} + \frac{1}{\tau_{p_j}}\right)^2}$$
$$+\left\{\frac{4}{\left(\frac{v_{p_j}}{\zeta}\right)^2 - \left(\frac{1}{\tau_{p_j}} + \frac{1}{\xi}\right)^2} - \frac{1}{\left(\frac{v_{p_j}}{\zeta} + \frac{1}{\tau_{p_j}} + \frac{1}{\xi}\right)^2}\right.$$
$$\left.-\frac{1}{\left(\frac{v_{p_j}}{\zeta} - \frac{1}{\tau_{p_j}} - \frac{1}{\xi}\right)^2}\right\}\frac{v_{p_j}}{2\zeta\left(\frac{1}{\tau_{p_i}} - \frac{1}{\xi} + \left(\frac{1}{\tau_{p_j}} + \frac{1}{\xi}\right)\frac{v_{p_i}}{v_{p_j}}\right)}$$
$$+\left\{\frac{2\zeta}{\left(\frac{v_{p_i}}{\zeta} + \frac{1}{\tau_{p_i}} + \frac{1}{\xi}\right)} - \frac{2\zeta}{\left(\frac{v_{p_j}}{\zeta} - \frac{1}{\tau_{p_j}} - \frac{1}{\xi}\right)}\right.$$
$$\left.-\frac{v_{p_i}}{\left(\frac{v_{p_i}}{\zeta} + \frac{1}{\tau_{p_i}} + \frac{1}{\xi}\right)^2} + \frac{v_{p_j}}{\left(\frac{v_{p_j}}{\zeta} - \frac{1}{\tau_{p_j}} - \frac{1}{\xi}\right)^2}\right\}$$
$$\times\frac{1}{2\zeta\left(\frac{v_{p_i}-v_{p_j}}{\zeta} + \frac{1}{\tau_{p_i}} + \frac{1}{\tau_{p_j}}\right)}, \quad (17)$$

and $\Psi(\xi,\zeta)$ is

$$\Psi(\xi,\zeta) = \frac{1}{\frac{1}{\tau_{p_k}} + \frac{1}{\xi} + \frac{v_{p_k}}{\zeta}} - \frac{v_{p_k}}{2\zeta\left(\frac{1}{\tau_{p_k}} + \frac{1}{\xi} + \frac{v_{p_k}}{\zeta}\right)^2}, \quad (18)$$

where $v_{p_k} = \frac{2\rho_w g r_k{}^2}{\rho_a \mu}$.

The RDF at contact $g_{ij}(r=R)$ is given by

$$g_{ij}(r=R) = \left(\frac{\eta^2 + r_c{}^2}{R^2 + r_c{}^2}\right)^{C_1/2}. \quad (19)$$

C_1 has the expression

$$C_1 = \frac{y(ST)}{(|\mathbf{g}|/(v_k/\tau_k))^{f(R_\lambda)}}, \quad (20)$$

where

$$y(ST) \;=\; -0.1988ST^4 + 1.5275ST^3 \\ -4.2942ST^2 + 5.3406ST,$$
$$f(R_\lambda) \;=\; 0.1886\exp\left(\frac{20.306}{R_\lambda}\right),$$

and $ST \equiv \max(St_2, St_1)$. The expression for r_c is given by

$$\left(\frac{r_c}{\eta}\right)^2 = |St_2 - St_1| F(a_{o_g}, R_\lambda),$$

where a_{o_g} is

$$a_{o_g} = a_o + \frac{\pi}{8}\left(\frac{|\mathbf{g}|}{v_k/\tau_k}\right)^2$$

and $F(a_{o_g}, R_\lambda)$

$$F(a_{o_g}, R_\lambda) = 20.115\left(\frac{a_{o_g}}{R_\lambda}\right)^{1/2}.$$

$f(R)$ in Eq. (16) is calculated as

$$f(R) \;=\; \frac{1}{2(1-2\chi^2)^{1/2}} \times$$
$$\left\{\left(1+\sqrt{1-2\chi^2}\right)\exp\left[-\frac{2R}{\left(1+\sqrt{1-2\chi^2}\right)L_e}\right]\right.$$
$$\left.-\left(1-\sqrt{1-2\chi^2}\right)\exp\left[-\frac{2R}{\left(1-\sqrt{1-2\chi^2}\right)L_e}\right]\right\}.$$

3..4 Comparison of different kernels

In this section, we compare the magnitudes of the five collection kernels we have introduced, namely, (1) the Hall kernel, (2) the ZWW-RW kernel, (3) the mZWWa kernel, (4) the mZWWb kernel, and (5) the Ayala kernel. The unit for the kernels in all plots to be discussed is cm^3/s.

Fig. 1 is a contour plot of the Hall kernel for different droplet-droplet size combinations. The contour plot is symmetric with respect to the 45^o line on which the Hall kernel becomes zero. The magnitude of the Hall kernel can vary by over 10 orders of magnitude from 1 μm to 1 mm, due to the large changes in both

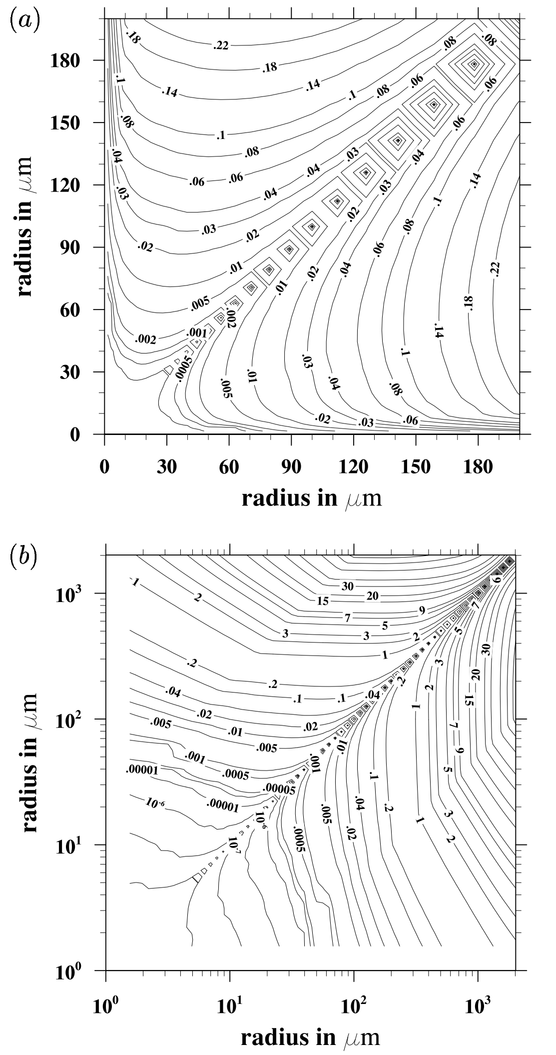

Figure 1: Contour plots of the Hall kernel: (a) linear size axes up to 200 μm; (b) logarithmic size axes up to 2 mm.

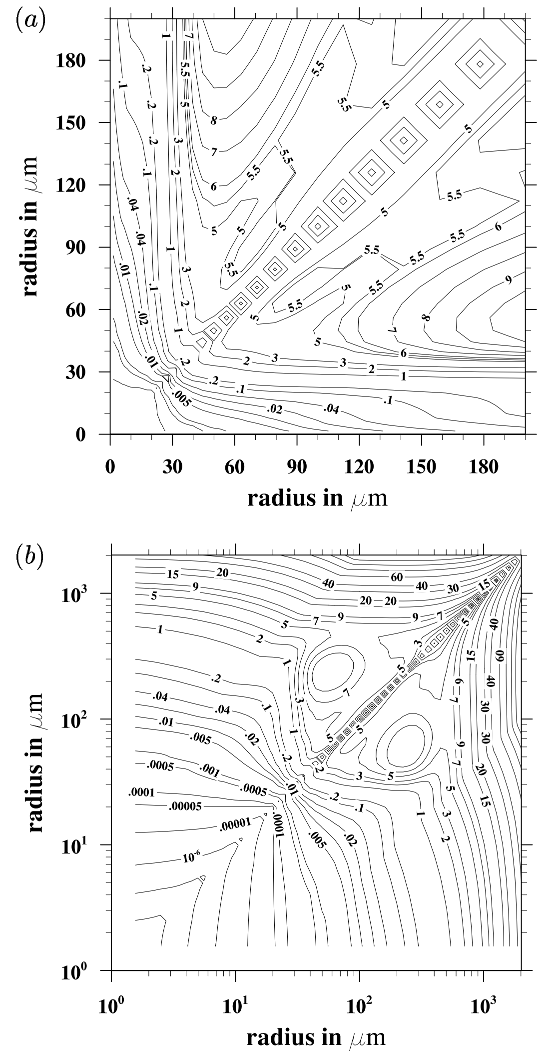

Figure 2: Contour plots of the ZWW-RW kernel shown in Eq. (11): (a) linear size axes up to 200 μm; (b) logarithmic size axes up to 2 mm. Here, $\epsilon = 300$ cm^{2}s^{-3} and $u' = 350$ cm/s.

collision efficiency and the terminal velocity. The Hall kernel is less than 0.03 cm^3/s for droplets less than 100 μm. For droplets larger than 100 μm in radius, the kernel is proportional to the differential sedimentation velocity, as the collision efficiency is close to one. If the larger droplet in the colliding pair is 1 mm in radius, the kernel may be on the order of 20 cm^3/s.

The contour plot for the ZWW-RW kernel is shown in Fig. 2. As noted by RW05, the turbulent contribution dominates the ZWW-RW kernel for droplet pairs whose sizes fall between 50 μm and about 500 μm. For example, the ZWW-RW kernel can be on the order of 5.0 cm^3/s when the larger droplet in the pair is 100 μm, which is larger than the Hall kernel by two orders of magnitude. For droplets smaller than 50 μm, the turbulent contribution is also much larger than the gravitational contribution due to the assumed unity collision efficiency in the former contribution but the realistic collision efficiency for the latter contribution (see Fig. 9 (a)). Berry and Reinhardt (1974) proposed three modes of growth of cloud droplets by collision-coalescence. After dividing the size spectrum into small cloud droplets (S1, roughly less than 50 μm) and larger drops (S2, roughly larger than 50 μm), Berry and Reinhardt showed that the initial growth is governed by $S1 - S1$ *autoconversion* to add water to S2, followed by *accretion* via $S2 - S1$ interactions, and eventually by $S2 - S2$ *large hydrometeor self-collection*. The contour plot (Fig. 2) implies that both the autoconversion and accretion rates are dramatically increased by the turbulent contribution in the ZWW-RW kernel. For droplets larger than 500 μm, the gravitational contribution is in general larger than the

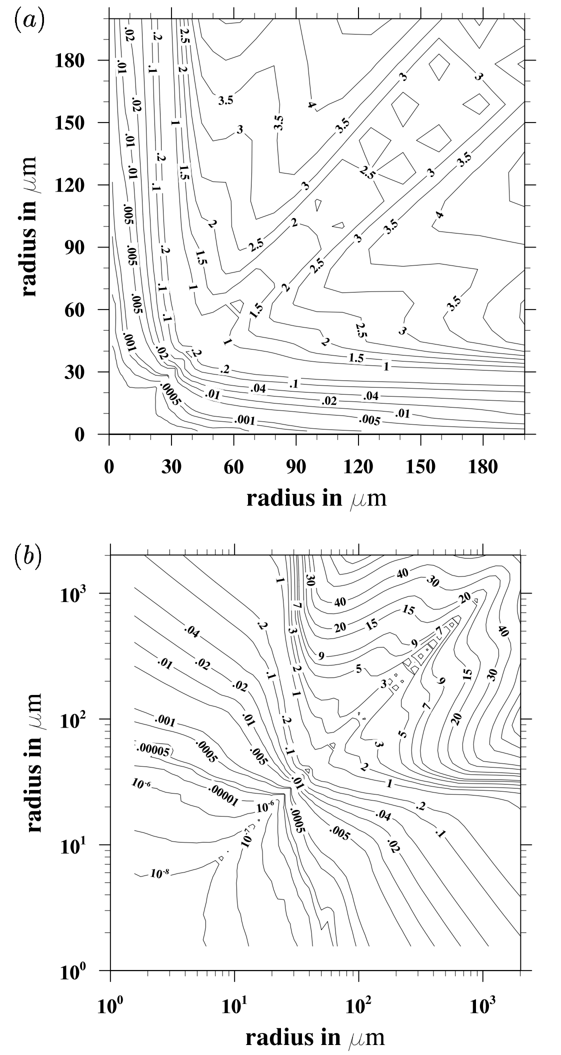

Figure 3: Contour plots of the mZWWa kernel: (a) linear size axes up to 200 μm; (b) logarithmic size axes up to 2 mm. Here, $\epsilon = 300$ cm^{2}s^{-3} and $u' = 350/\sqrt{3}$ cm/s.

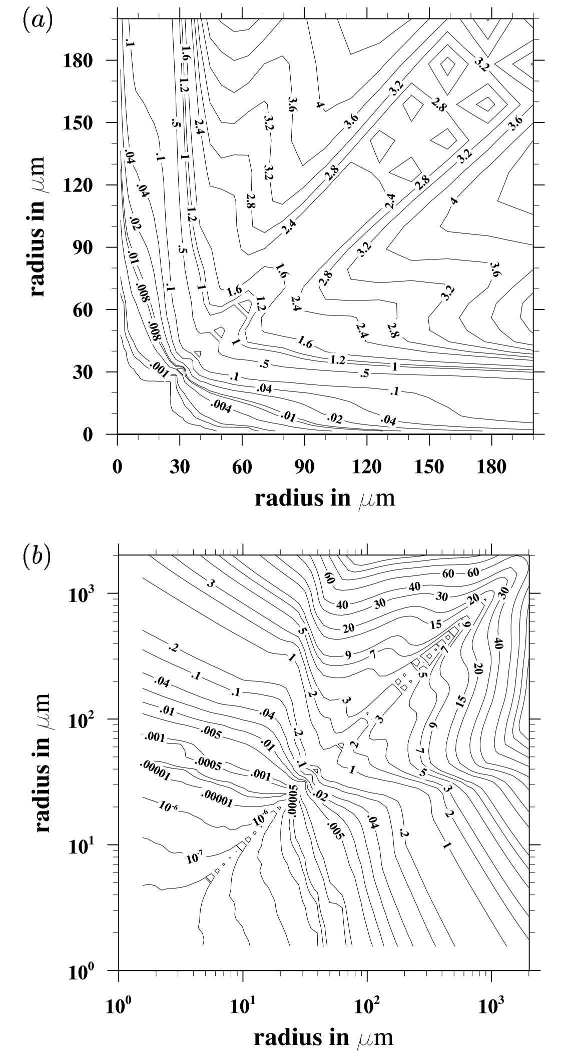

Figure 4: Contour plots of the mZWWb kernel shown in Eq. (12): (a) linear size axes up to 200 μm; (b) logarithmic size axes up to 2 mm. Here, $\epsilon = 300$ cm^{2}s^{-3} and $u' = 350/\sqrt{3}$ cm/s.

turbulent contribution. It must be noted that the turbulent contribution in the ZWW-RW kernel is grossly overestimated (Wang *et al.* 2006a).

The contour plots for the mZWWa kernel and the mZWWb kernel are displayed in Fig. 3 and Fig. 4, respectively. The mZWWa kernel is in general smaller than the ZWW-RW kernel for droplets less than 100 μm due to the use of the nonlinear drag and the small fluid rms fluctuation velocity. For example, the mZWWa kernel is about half the value of the ZWW-RW kernel for droplets pairs whose larger droplet is 100 μm in radius. However, it appears that the mZWWa kernel is larger than the ZWW-RW kernel for droplets on the order of 1 mm, as a result of the much slower decay of the radial distribution function with increasing droplet size due to the nonlinear drag (see Fig. 6). In fact, the radial distribution function (RDF) may remain much larger than one when the terminal velocity reaches a constant value for droplets larger than 2 mm in radius (which also implies a constant effective inertial response time). This slow decay is physically incorrect since the model for RDF here was derived from ZWW01 without the influence of sedimentation (e.g., Wang et al. 2006). Also it appears that the mZWWa kernel is larger than the Hall kernel if both colliding droplets are larger than 30 μm, see Fig. 9 (b). If one of droplets in the pair is less than 30 μm, however, the mZWWa is less than the Hall kernel. This implies that both the autoconversion from droplets less than 30 μm and the capturing of small cloud droplets by large drops through accretion (Berry and Reinhardt 1974) for the mZWWa kernel is slower than in the Hall

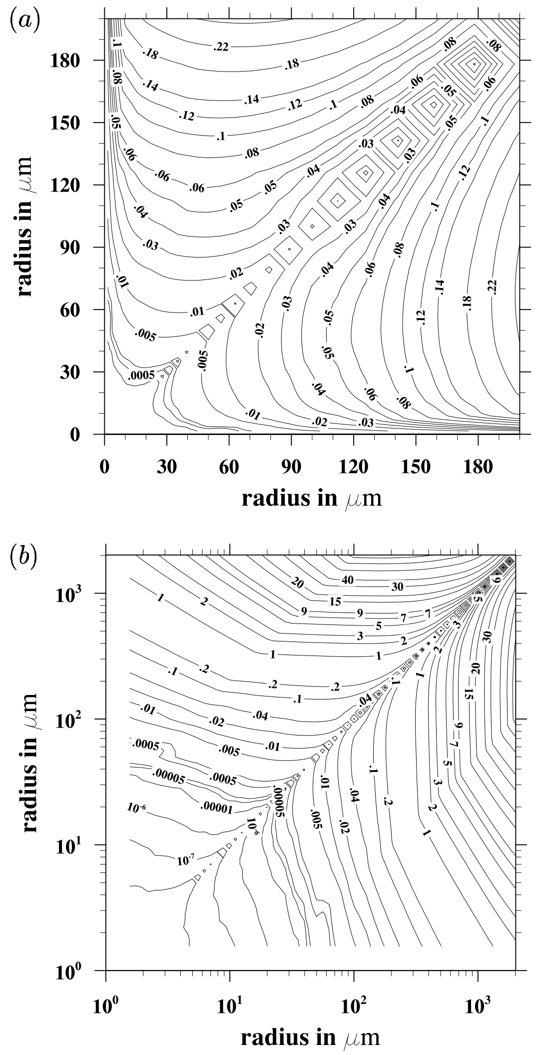

Figure 5: Contour plots of the Ayala kernel: (a) linear size axes up to 200 μm; (b) logarithmic size axes up to 2 mm. Here, $\epsilon = 300$ cm^{2}s^{-3} and $u' = 350/\sqrt{3}$ cm/s.

kernel.

The mZWWb kernel is very similar to the mZWWa kernel for most size combinations, except that, by definition, the mZWWb kernel is always larger than the Hall kernel (see Fig. 9 (c)). Therefore, the accretion mode is still effective for the mZWWb kernel.

The contour plot for the Ayala kernel is shown in Fig. 5. Compared to the other turbulent collection kernels considered above, the Ayala kernel shows a much less dramatic enhancement by air turbulence, but at the same time, the enhancement appears for all droplets less than 100 μm. The effect of air turbulence is negligible for droplets larger than 100 μm in the Ayala kernel. This is very different from the other turbulent collection kernels. This is a result of the assumed vanishing preferential concentration in the Ayala kernel for droplets larger than 100 μm, as the effect of sedimentation on the RDF is actually considered in the Ayala kernel. The distribution of RDF over droplet size in the Ayala kernel is much more localized than that in the other turbulent kernels, see for example, Fig. 7 for the mZWWa kernel as compared to Fig.8 for the Ayala kernel.

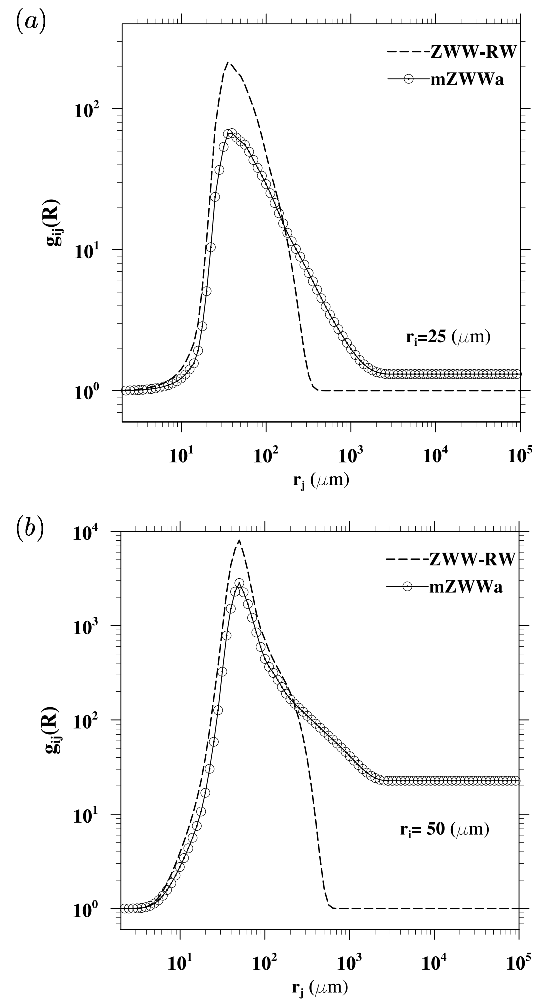

Figure 6: Comparison of radial distribution function (RDF), $g_{ij}(R)$, in the mZWWa kernel and in the ZWW-RW kernel for different r_i. $g_{ij}(R)$ in the mZWWa kernel is calculated based on the nonlinear drag force with the turbulent parameter $\epsilon = 300$ cm^{2}s^{-3} and $u' = 350/\sqrt{3}$ cm/s. $g_{ij}(R)$ in the ZWW-RW kernel is calculated based on the Stokes drag with the turbulent parameter $\epsilon = 300$ cm^{2}s^{-3} and $u' = 350$ cm/s.

We would like to point out that the turbulent contribution in the ZWW-RW, mZWWa, and mZWWb kernels contains the effect of preferential concentration as quantified by RDF, which tend to create an internal region with a maximum local collection kernel. For example, in Fig. 2 for the ZWW-RW kernel, this maximum happens when $100\ \mu m < r_1 < 400\ \mu m$ and $r_2 \approx 50\mu m$. In the case of the mZWWa kernel shown in Fig. 3(b), the maximum occurs along two tilted lines with angles at 10^o and 30^o. Similar internal regions are found in the mZWWb kernel shown in Fig. 4(b), but with smaller angles due to the addition of the gravitational kernel. The Ayala kernel also shows the maxima along the line of about 10^o to 15^o angle. This type of internal local maxima is a result of the combined effect of RDF and the radial relative velocity. The maximum in RDF tends to occur for droplet pairs of similar sizes or along the 45^o line in the contour plots, while the radial relative velocity obtains its maximum along the 0^o line in the contour plots. The internal maximum regions would not occur if the preferential concentration is not present, such as in the Hall kernel. As a further demonstration of this, we plot in Fig. 7 and Fig. 8 the RDF, radial relative velocity, and their product as a function of r_2 with two fixed values of r_1, for the mZWWa kernel and the Ayala kernel, respectively. The plots show that the peak in RDF could cause local maxima in the product at locations shifted from the peak location of the RDF.

As a summary, Fig. 9 compares the ratios of the turbulent collision kernels to the based Hall kernel. These ratios reflect the level of enhancement by the air turbulence, relative to the based Hall kernel. The ratio of the mZWWb and the ratio of mZWWa are pretty similar (see Fig. 9(b) and Fig. 9(c)) except the ratios of mZWWb are all greater than one. The ZWW-RW kernel has much greater ratio value than the mZWWb. One reason is the assumed unit collision efficiency for the turbulent part in the ZWW-RW kernel, while the mZWWb kernel uses the collision efficiency in the Hall kernel, which partially accounts for the gravitational-hydrodynamical interactions. Another reason is the different u' values used in these two different kernels. The typical range of rms airflow velocity should be from 0.5 m/s to 2.0 m/s according to observations (Weil and Lawson 1993; Smith and Jonas 1995, Furomoto *et al.* 2003). RW05 incorrectly used $u' = 350$ cm/s, a factor of $\sqrt{3}$ larger than reality (*e.g.*, see reply by Riemer and Wexler 2006). Therefore, the ZWW-RW kernel greatly overestimates the turbulent contribution relative to the gravitational contribution. Compared with the other three turbulent collision kernels, the Ayala kernel has smaller ratio ranges. The white blank areas mean that the ratio in those area is pretty close to one or equal to one. In the square area of radius from zero to 30 μm, the ratio of mZWWb's is less than Ayala's. Equally, the magnitude of mZWWb is less than the Ayala kernel in this square area and in the other areas except this small square mZWWb is larger than the Ayala kernel.

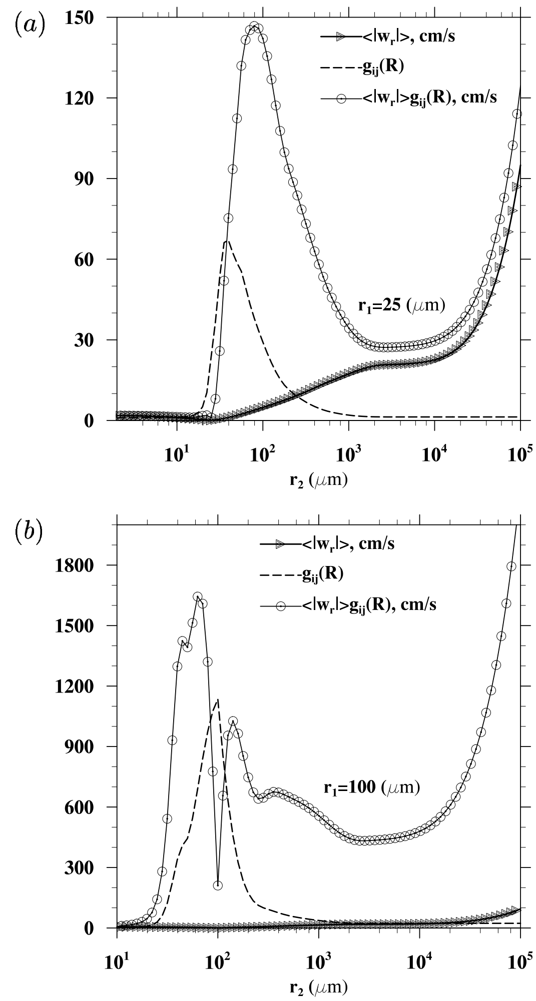

Figure 7: The radial relative velocity and the radial distribution function as a function of r_2 with (a)$r_1 = 25\ \mu$m and (b)$r_1 = 100\ \mu$m in the mZWWa kernel. Here, $\epsilon = 300$ cm^{2}s^{-3} and $u' = 350/\sqrt{3}$ cm/s.

4. Effect of turbulent collision kernels on the size evolution of cloud droplets

We shall now examine the droplet size distributions at different times and compare the results for the five different kernels discussed in the last section. The following initial condition

$$n(x, t=0) = \frac{N_0}{\bar{x}_{f0}} \exp(-\frac{x}{\bar{x}_{f0}}), \text{ or}$$
$$g(\ln r, t=0) = 3L_0(\frac{x}{\bar{x}_{f0}})^2 \exp(-\frac{x}{\bar{x}_{f0}}) \qquad (21)$$

is assumed. The liquid water content is set to $L_0 = 1\ g/m^3$ and the initial mean mass $\bar{x}_{f0} \equiv L_0/N_0 = 3.3 \times 10^{-12}$ kg or the corresponding mean radius $\bar{r}_{f0} \equiv (3\bar{x}_{f0}/4\pi\rho_w)^{1/3} = 9.3\ \mu$m.

The integral form of the kinetic collection equation is solved by a recently developed bin integral method with Gauss Quadrature (BIMGQ, Xue 2006).

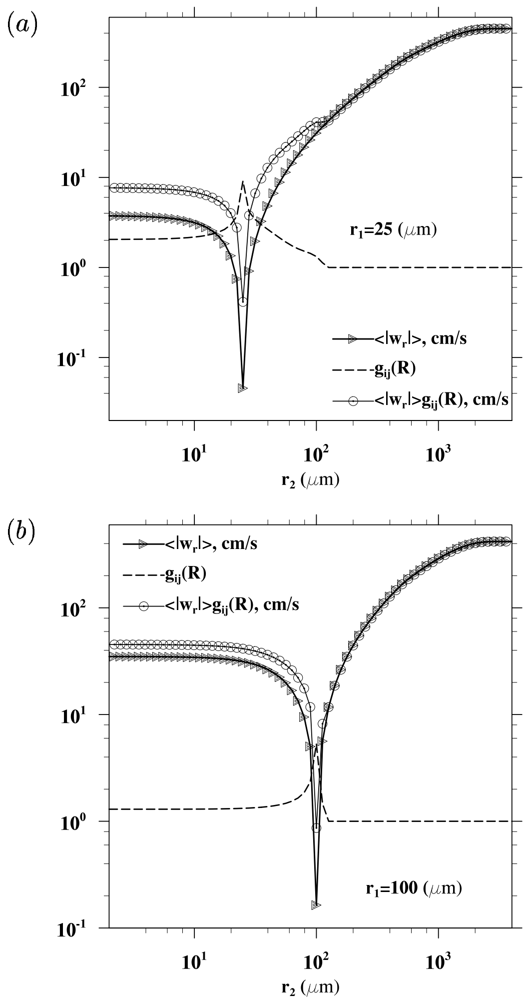

Figure 8: The radial relative velocity and the radial distribution function as a function of r_2 with (a)$r_1 = 25$ μm and (b)$r_1 = 100$ μm in the Ayala kernel. Here, $\epsilon = 300$ cm^{2}s^{-3} and $u' = 350/\sqrt{3}$ cm/s.

BIMGQ utilizes an extended linear bin-wise distribution and the concept of pair-interaction to redistribute the mass over new size classes as a result of collision-coalescence. Xue (2006) compared the method with existing numerical approaches for KCE including the method of Berry and Reinhardt (1974), the linear flux method of Bott (1998), and the linear discrete method of Simmel *et al.* (2002). She showed that BIMGQ has a comparable or better accuracy and convergence behavior and is computationally efficient. Here we used a small bin mass ratio of $\alpha = 2^{1/4}$ to ensure a very accurate numerical integration of the KCE by BIMGQ (23).

First, we plot in Fig. 10 to Fig. 11 the mass density distribution of cloud droplets every 10 minutes after the initial time, on both linear and logarithmic scales. Five curves in each plot represent five different collection kernels. Clearly, the ZWW-RW kernel produces the fastest growth, with the second peak at larger size, resulting from the accretion mode, appearing before 10 min. On the other hand, the mZWWa kernel results in the slowest growth and only produces a very weak secondary peak at $t = 60$ min. The other three kernels all generate the secondary peak. At $t = 30$ min, the percentage of mass for droplets larger than 100 μm is 93%, 76%, 60%, 0.32%, and 0% for the ZWW-RW kernel, the Ayala kernel, the mZWWb kernel, the Hall kernel, and the mZWWa kernel, respectively. This clearly shows the impact of air turbulence in generating drizzle droplets and that the gravitational mechanism alone is not sufficient.

As indicated earlier, there are roughly three phases of growth (Berry and Reinhardt 1974): (1) the autoconversion phase in which the self-collections of the small cloud droplets near the peak of the initial size distribution slowly shift the initial peak of the size distribution and, at the same time, transfer mass to larger size by a weak accretion mechanism; (2) the accretion phase in which the accretion mode dominates over the autoconversion mode and serves to quickly transfer mass from the initial peak to the newly formed secondary peak at a larger size; and (3) the large hydrometeor self-collection (LHSC) phase in which the self-collections of large droplets near the second peak now dominate over the the accretion mode, as the initial peak is diminishing and the second peak is gaining strength.

We shall now develop a method to identify these three phases by plotting the net rate of transfer of mass density in each bin, $dg(\ln r)/dt$. Fig. 12(b) displays the distribution of $dg(\ln r)/dt$ every 10 minutes for the case of the Ayala kernel. A more detailed plot for every one minute is shown in Fig. 13 for the same kernel. This net rate of transfer was directly solved in the BIMGQ approach. It is noted that $dg(\ln r)/dt$ can be either positive and negative, with a total integral over the whole size range equal to zero according to the mass conservation. At any given time, a positive $dg(\ln r)/dt$ for a given size bin implies that the mass density for that size bin is gaining mass. The three phases are clearly visible in Fig. 13. During Phase 1, $dg(\ln r)/dt$ is non-zero mainly near the initial peak of the size distribution, with a negative region immediately followed by a positive region in $dg(\ln r)/dt$. Phase 2 is characterized by a largely negative region of $dg(\ln r)/dt$ near the initial peak and a largely positive region of $dg(\ln r)/dt$ near the newly formed, second peak. There is a size gap in between the two regions during Phase 2, showing that the accretion mode can directly move mass from smaller droplets to droplets much larger in size. Finally, $dg(\ln r)/dt$ is non-zero mainly near the second peak during the LHSC phase, again with a negative region immediately followed by a positive region in $dg(\ln r)/dt$.

To unambiguously identify the time intervals for the three phases, we plot in Fig. 14, as a function of time, the location in size, $r_{\max}$, corresponding to the maximum $dg(\ln r)/dt$ and the location in size, $r_{\min}$,

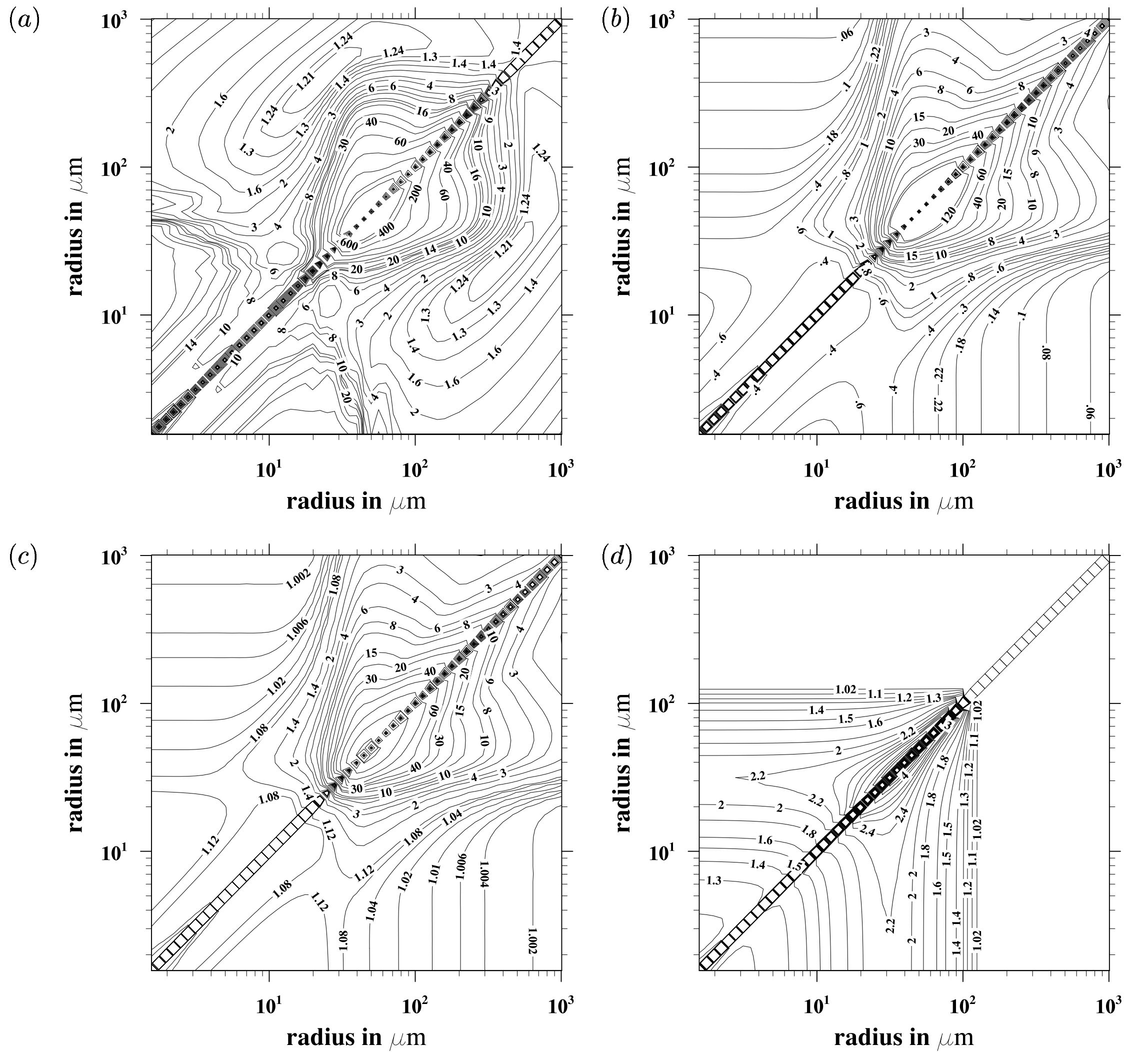

Figure 9: Ratios of different collision kernels to the Hall kernel: (a) the ratio of the ZWW-RW kernel to the Hall kernel; (b) the ratio of the mZWWa kernel to the Hall kernel; (c) the ratio of the mZWWb kernel to the Hall kernel; (d) the ratio of the Ayala kernel to the Hall kernel. Here, $\epsilon = 300$ cm^{2}s^{-3} and $u' = 350/\sqrt{3}$ cm/s for the mZWWa kernel, the mZWWb kernel, and the Ayala kernel. $\epsilon = 300$ cm^{2}s^{-3} and $u' = 350$ cm/s for the ZWW-RW kernel.

corresponding to the minimum $dg(\ln r)/dt$ for the 61 curves shown in Fig. 13. Only times at every one-minute separation are considered. The maximum and minimum values of $dg(\ln r)/dt$ are also shown in Fig. 14(b). For the Ayala kernel, Fig. 14(a) shows that $r_{\max}$ experiences a sudden jump at about $t = 14.5$ min. This time marks the end of Phase 1 and the begin of Phase 2. Then at about $t = 29.5$ min, $r_{\min}$ shows a sudden increase and this time marks the end of the Phase 2 and the begin of the Phase 3. These transition times correspond well with the detailed $dg(\ln r)/dt$ curves in Fig. 13. Furthermore, while both the maximum value and the minimum value of $dg(\ln r)/dt$ remain roughly the same for Phase 1, the maximum value of $dg(\ln r)/dt$ grows rapidly during Phase 2 when the accretion mode is switched on. The magnitude of the minimum $dg(\ln r)/dt$ also grows initially during Phase 2, but reaches a peak and then drops during the late part of the accretion phase, as a result of diminishing mass content of small cloud droplets. The magnitudes of the maximum and minimum $dg(\ln r)/dt$ in general decay during the third phase.

The same procedure was applied to the results based on the other four kernels to identify the time interval corresponding to each phase. The results are summarized in Table 1. As far as the generation of drizzle drops, the initiation of the accretion phase is a critical step. The time for the initiation of the accretion phase is about 6.5 min, 14.5 min, 24.5 min, 32.5 min, 51.5 min for the ZWW-RW kernel, the Ayala kernel, the mZWWb kernel, the Hall kernel, and the mZWWa ker-

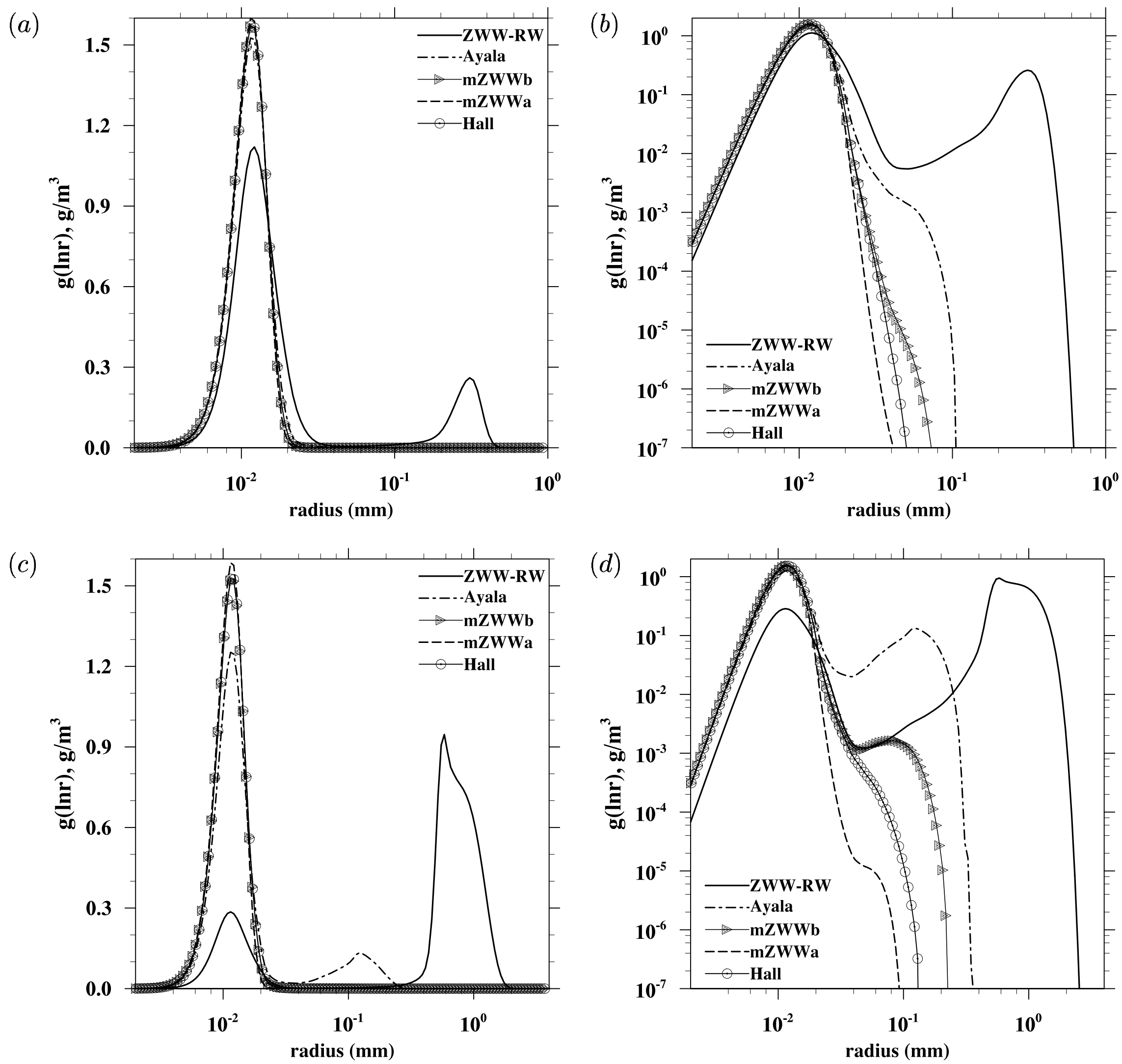

Figure 10: Mass density distributions: (a) $t = 10$ min; (b) $t = 10$ min with logarithmic scale; (c) $t = 20$ min; (d) $t = 20$ min with logarithmic scale. Here, the bin resolution is $\alpha = 2^{1/4}$. The initial condition is given by Eq. (21).

nel, respectively. This again shows that air turbulence can significantly reduce the time for the initiation of the accretion phase, and the order is consistent with the observed speed of growth shown in Fig. 10 to Fig. 11. This is intimately related to the effectiveness of the autoconversion mechanism in Phase 1. Noticeably is the fact that, although the Ayala kernel does not produce a very large enhancement in the collection kernel compared to the ZWW-RW kernel, it still is very effective in shortening the time for Phase 1. Namely, the magnitude of the enhancement of the collection kernel is not the most important factor, but the location of the enhancement of the collection kernel by air turbulence is more relevant. If the air turbulence can promote the collection kernel involving small droplets, the autoconversion rate is enhanced so that the accretion phase can be triggered earlier. Once the accretion phase sets in, the gravitational mechanism will take over to continue the growth process. In the absence of the gravitational mechanism such as in the mZWWa kernel, the autoconversion phase takes too long to set up the accretion phase, which makes it almost impossible to grow drizzle drops within a reasonable time.

Therefore, it turns out that the magnitude of the autoconversion rate during the early part of the time evolution determines the initiation time for drizzle drops. Fig. 15 shows how the time interval $T_{\rm auto}$ for the autoconversion phase is inversely related to the maximum magnitude of dg/dt at $t = 0$ (this maximum magnitude is also listed in Table 1). The distributions of $dg(\ln r)/dt$ at $t = 0$ are also shown in Fig. 12 (a) for comparison between different kernels. The correlation

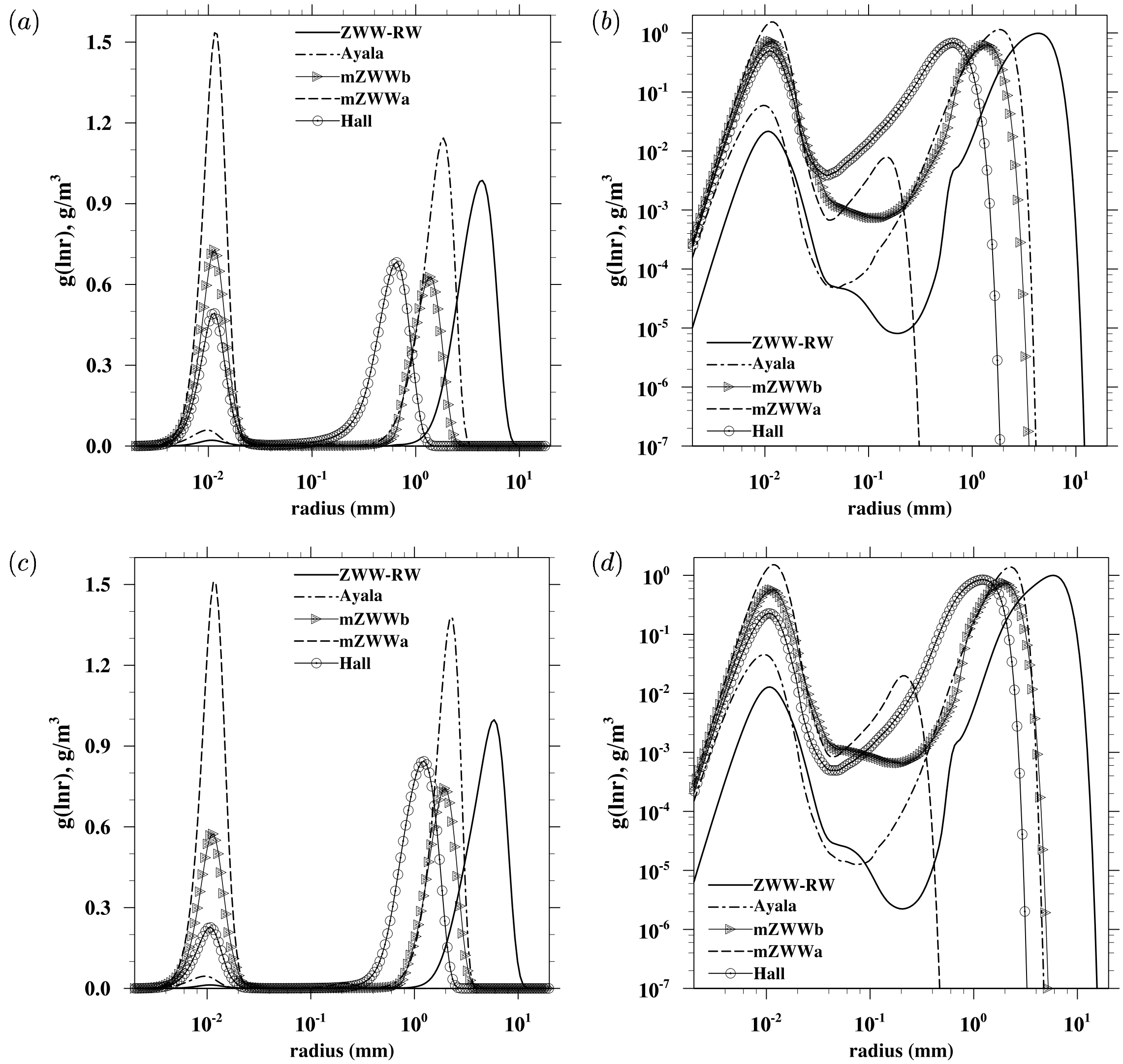

Figure 11: Mass density distributions: (a) $t = 50$ min; (b) $t = 50$ min with logarithmic scale; (c) $t = 60$ min; (d) $t = 60$ min with logarithmic scale.

may be fitted as

$$T_{\text{auto}} = 0.07 \times \left(\frac{dg}{dt}\right)_{\max}^{-2/3}. \tag{22}$$

This inverse relation again shows the importance of the autoconversion mode. At this point, it is not completely clear what conditions trigger the accretion phase.

Alternative ways of monitoring the growth process are shown in Fig. 16 and Fig. 17. First, the radar reflectivity in dBZ (see Introduction) is shown in Fig. 16(a) for the five kernels. The order of the speed of the growth is shown to be the same as before. An interesting observation is that the rapid growth phase corresponds exactly to the same time interval for the accretion phase shown in Table 1. Fig. 16(b) shows the time evolution of the droplet radius r_g corresponding to the mean mass based on the mass density distribution, according to Berry and Reinhardt (1974). r_g describes roughly the location of the second peak at the larger size. The time evolution of r_g is rather similar to that of radar reflectivity.

Finally, the percentage of mass in the mass distribution for droplets larger than $50\ \mu m$ in radius is shown in Fig. 17(a) and the percentage of mass for droplets in the size range from $20\ \mu m$ to $100\ \mu m$ is shown in Fig. 17(b). The rapid growth phase in Fig. 17(a) and the occurrence of the peak in Fig. 17(b) follow the same similar order for the five different kernels.

Four characteristic times are extracted from Fig. 16 and Fig. 17 and they are listed in Table 2, including the time t_1 when dBZ reaches 20, the time t_2

Table 1: The time interval for each growth phase of the cloud droplets.

kernel	Phase 1	Phase 2	Phase 3	$\left[\frac{dg}{dt}\right]_{max}(t=0)$ (g/m^3)
Hall kernel	$t < 32.5$ min	32.5 min $< t < 51.5$ min	$t > 51.5$ min	0.138e-3
mZWWa kernel	$t < 51.5$ min	$t > 51.5$ min	-	0.0465e-3
mZWWb kernel	$t < 24.5$ min	24.5 min $< t < 38.5$ min	$t > 38.5$ min	0.146e-3
Ayala kernel	$t < 14.5$ min	14.5 min$< t < 29.5$ min	$t > 29.5$ min	0.267e-3
ZWW-RW kernel	$t < 6.5$ min	6.5 min$< t < 12.5$ min	$t > 12.5$ min	1.160e-3

- Phase 1. Autoconversion
- Phase 2. Accretion
- Phase 3. Hydrometeor self-collection

when r_g reaches 200 μm, the time t_3 when at least 50% of the mass is contained by droplets larger than 50 μm, and t_4 when the percentage of mass in the intermediate size range from 20 μm to 100 μm reaches the maximum. Comparing the data in Table 2 with the data in Table 1, we find that t_1, t_2, and t_4 all fall within the corresponding time interval for the accretion phase. The value of t_3 belongs either in the late part of the accretion phase or the early part of the LHSC phase.

The above calculation was based on one flow dissipation rate. We repeated the calculation for the 4 different turbulent kernels for several different flow dissipation rates and three different flow rms fluctuation velocities. In Table 3, we compare the resulting values of t_1 and t_2. Both t_1 and t_2 decrease with increasing the dissipation rate at a fixed flow fluctuation velocity or with increasing fluctuation velocity at a fixed dissipation rate. These reflect that the stronger the air turbulence, the shorter is the time needed to form the drizzle drops. Fig. 18 compares t_1 and t_2 with our base case, the Hall kernel, which only considers the gravitational mechanism. The same observations can be made. We also list in Table 3 the percentage of reduction in t_1 and t_2 when compared with the base case. Compared with the base case, the air turbulence can shorten the time for the formation of drizzle drops roughly from 20% to 45% when the dissipation rate varies from 100 cm^2/s^3 to 400 cm^2/s^3 with the range of r.m.s. velocity considered.

Table 2: Characteristic times for the growth of cloud droplets.

kernel	t_1 (s)	t_2 (s)	t_3 (s)	t_4 (s)
Hall kernel	2448	2122	2804	2400
mZWWa kernel	-	-	-	-
mZWWb kernel	1913	1630	3070	1860
Ayala kernel	1498	1227	1536	1320
ZWW-RW kernel	640	440	883	600

- t_1 is the time at which dBZ reaches 20.
- t_2 is the time at which r_g=200 μm. r_g is the radius corresponding to the mass averaged mean mass x_g (Berry and Reinhardt 1974).
- t_3 is the time that the total mass of droplets with radius more than 50 μm is 50 % of the total mass, taken from Fig. 17(a).
- t_4 is the time corresponding to the maximum mass percentage of droplets with radius from 20 μm to 100 μm, taken from Fig. 17(b).

5. SUMMARY

In summary, we studied the impact of air turbulence on the growth of cloud droplets using new collision kernel parametrization and an accurate bin inte-

Table 3: Characteristic times for the growth of cloud droplets under different turbulent dissipation rate and fluctuation velocity combinations.

ϵ (cm^2/s^3)	u' (cm/s)	t_1 (s)	t_2 (s)	Reduction of t_1,%	Reduction of t_2,%
100	100	1949	1632	20.4	23.1
	150	1832	1517	25.2	28.5
	202	1738	1445	29.0	31.9
200	100	1816	1521	25.8	28.3
	150	1685	1400	31.2	34.0
	202	1584	1288	35.3	39.3
300	100	1736	1462	29.1	31.1
	150	1602	1339	34.6	36.9
	202	1498	1227	38.8	42.2
400	100	1681	1411	31.3	33.5
	150	1547	1287	36.8	39.3
	202	1443	1174	41.1	44.7

- t_1 is the time at which dBZ reaches 20.
- t_2 is the time at which r_g=200 μm. r_g is the radius corresponding to the mass averaged mean mass x_g (Berry and Reinhardt 1974).
- The reduction percentage is calculated based on the t_{1H}, and t_{2H}, the t_1 and t_2 for the Hall kernel, respectively. For example, the reduction of t_1 is equal to $(t_{1H} - t_1)/t_{1H}$.
- The data are calculated according to the Ayala kernel.

gral method for KCE. Based on the recent studies by Wang *et al.* (1998), Zhou *et al.* (2001), Riemer and Wexler (2005), and Ayala (2005), we considered four different turbulent collision kernels and compare several time scales for warm rain initiation relative to the hydrodynamical-gravitational kernel of Hall (1980). We only consider the effects of air turbulence on the geometric collision kernel through local flow shear, local fluid acceleration, and preferential concentration.

The general observation is that the time evolution of the growth process is quite similar for the Ayala kernel, the mZWWb kernel, and the Hall kernel, except that the three kernels result in different times for the switch from the autoconversion phase to the accretion phase to take place. If we take the Ayala kernel as the most appropriate kernel for the description of collision-coalescence rate in clouds, then the air turbulence can shorten the time for the formation of drizzle drops by 39% based on t_1 or 42% based on t_2, when compared with the base case (the Hall kernel). This does not include the effect of air turbulence on the collision efficiency. Wang *et al.* (2006b) speculated that the combined effect of air turbulence on the geometric collision rate and collision efficiency can lead to at least a factor of two speedup in the warm rain initiation as compared to the gravitational mechanism alone. In general, we expect the gravity is still the dominate mechanism for collision-coalescence for droplets large than 60 μm. Without gravity, air turbulence alone (as in mZWWa) is not capable of producing rain in a reasonable time interval.

We also developed a novel method to unambiguously identify the time intervals for the three phases of collection growth as defined qualitatively by Berry and Reinhardt (1974). We used the maximum and minium of the net mass-density transfer rate to locate the time intervals of the three phases. We found that the air turbulence have the strongest impact on the autoconversion phase, which is typically the longest phase for warm rain initiation. The overall implication is that a moderate increase of collection kernel of small droplets by air turbulence can have a significant impact on the warm rain initiation. At this stage, much remains to be done to accurately quantify the effects of air turbulence on collision rate and collision efficiency.

Acknowledgments This study has been supported by the National Science Foundation through grants ATM-0114100 and ATM-0527140, and by the National Center for Atmospheric Research (NCAR).

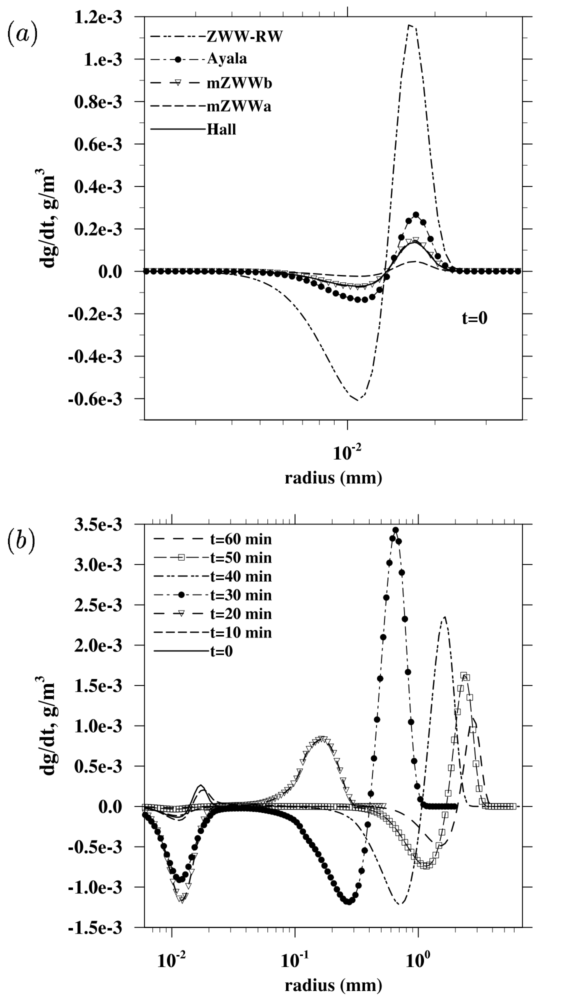

Figure 12: (a) dg/dt at the initial time $t = 0$ for different collision kernels; (b) dg/dt distributions at different simulation times for the Ayala kernel.

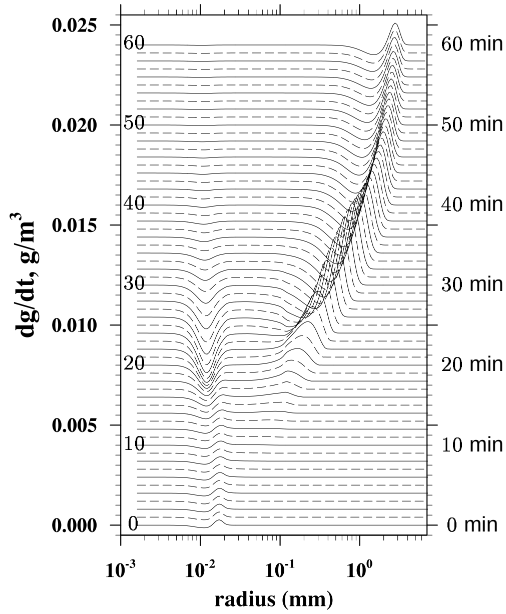

Figure 13: dg/dt distributions for the Ayala kernel at different times with a time spacing of 1 min.

References

[1] Ayala O., 2005: Effects of turbulence on the collision rate of cloud droplets. *Ph.D. Thesis*.

[2] Ayala O., Wang L-P, and Grabowski W.W., 2006: A hybrid approach for simulating turbulent collisions of hydrodynamically-interacting particles. *J. Comput. Phys.* (submitted).

[3] Beard K.V. and Ochs H.T., 1993: Warm-rain initiation: An overview of microphysical mechanisms. *J. Appl. Meteorol.*, **32**, 608-625.

[4] Berry, E.X. and R.I. Reinhardt, 1974: An analysis of cloud droplet growth by collection: Part I. Double distributions. *J. Atmos. Sci.*, **31**, 1814-1824.

[5] Bott A., 1998: A flux method for the numerical solution of the stochastic collection equation. *J. Atmos. Sci.*, **55**, 2284-2293.

[6] Furomoto J., Kurimoto K., and Tsuda T., 2003: Continuous observations of humidity profiles with the MU radar-RASS combined with GPS and radiosonde measurements. *J. Atmos. and Oceanic Tech.*, **20**, 23-41.

[7] Hall W.D., 1980: A detailed microphysical model within a two-dimensional dynamic framework: Model description and preliminary results. *J. Atmos. Sci.*, **37**, 2486-2507.

[8] Jonas P.R., 1996: Turbulence and cloud microphysics. *Atmos. Res.*, **40**, 283-306.

[9] Pinsky M., Khain A., and Shapiro M., 1997: Turbulence effects on droplet growth and size distribution in clouds - A review. *J. Aero. Sci.*, **28**, 1177-1214.

[10] Pruppacher H.R. and Klett J.D., 1997: *Microphysics of clouds and precipitation*. Kluwer Academic Publishers, 954 pages.

[12] Riemer N. and Wexler A.S., 2005: Droplets to drops by turbulent coagulation. *J. Atmos. Sci.*, **62**, 1962-1975.

[12] Riemer N. and Wexler A.S., 2006: Reply to Comments on “Droplets to drops by turbulent coagulation”. *J. Atmos. Sci.*, in press. *J. Atmos. Sci.*, **62**, 1962-1975.

[13] Shaw R.A., 2003: Particle-Turbulence Interactions in Atmospheric Clouds. *Annu. Rev. Fluid Mech.*, **35**, 183-227.

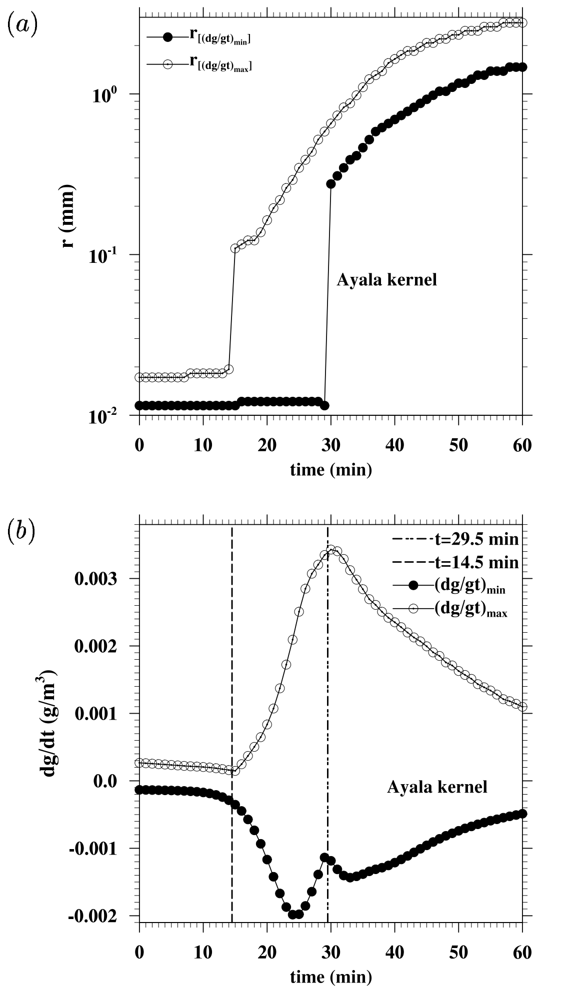

Figure 14: (a) The droplet radius corresponding to the maximum and minimum of dg/dt as a function of time for the Ayala kernel. (b) The maximum and minimum magnitude of dg/dt for the Ayala kernel.

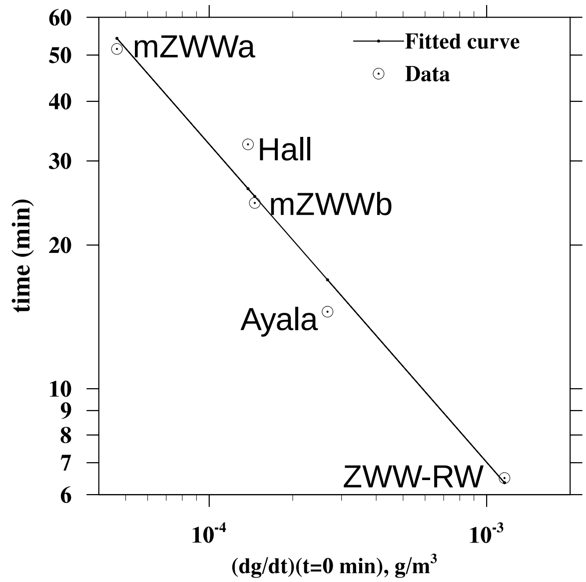

Figure 15: The time duration for the autoconversion phase (T_{auto}) as a function of the maximum magnitude of dg/dt at $t = 0$.

[14] Simmel M., Trautmann T., and Tetzlaff G, 2002: Numerical solution of the stochastic collection equation—-comparison of the linear discrete method with other methods. *Atmos. Res.*, **61**, 135-148.

[15] Smith S.S. and Jonas P.R., 1995: Observations of the turbulent fluxes in fields of cumulus clouds. *Q. J.R. Met. Soc.*, **121**, 1185-1208.

[16] Vaillancourt P.A. and Yau M.K., 2000: Review of particle-turbulence interactions and consequences for cloud physics. *Bull. Amer. Meteor. Soc.*, **81**, 285-298.

[17] Wang, L.P., Wexler A.S., and Zhou Y., 2000: Statistical mechanical description and modelling of turbulent collision of inertial particles. *J. Fluid Mech.*, **415**, 117-153.

[18] Wang L.P., Ayala O., and Grabowski W. W., 2005a: Improved formulations of the superposition method. *J. Atmos. Sci.*, **62**, 1255-1266.

[19] Wang L.P., Ayala O., Kasprzak S.E., and Grabowski W. W., 2005b: Theoretical formulation of collision rate and collision efficiency of hydrodynamically-interacting cloud droplets in turbulent atmosphere. *J. Atmos. Sci.*, **62**, 2433-2450.

[20] Wang L.P., Ayala O., Xue Y., and Grabowski W. W., 2006a: Comments on "Droplets to drops by turbulent coagulation". *J. Atmos. Sci.*, in press.

[21] Wang L.P., Xue Y., Ayala O., and Grabowski W. W., 2006b: Effects of stochastic coalescence and air turbulence on the size distribution of cloud droplets. *Atmos. Res.*, in press.

[22] Weil J.C. and Lawson R.P., 1993: Relative dispersion of ice crystals in seeded cumuli. *J. Appl. Met.*, **32**, 1055-1073.

[23] Xue, Y., 2006: Effects of air turbulence and stochastic coalescence on the size distribution of cloud droplets, Ph.D. dissertation, University of Delaware, Newark, DE, USA.

[24] Zhou Y., Wexler A.S., and Wang L.P., 2001: Modelling turbulent collision of bidisperse inertial particles. *J. Fluid Mech.*, **433**, 77-104.

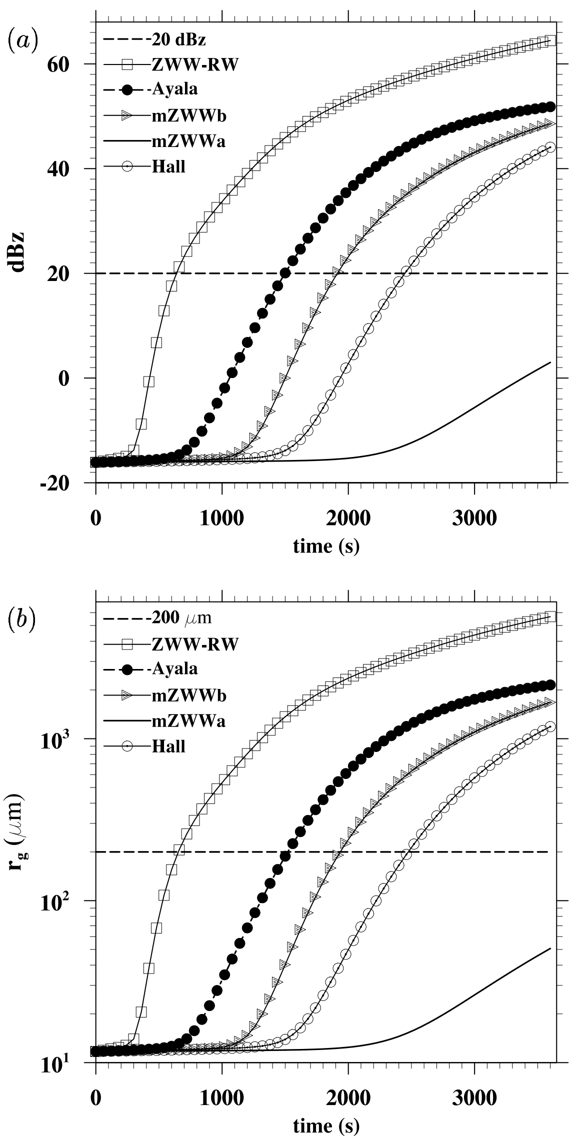

Figure 16: (a) dBZ as a function of time; (b) Mass-weighted mean radius (r_g) as a function of time.

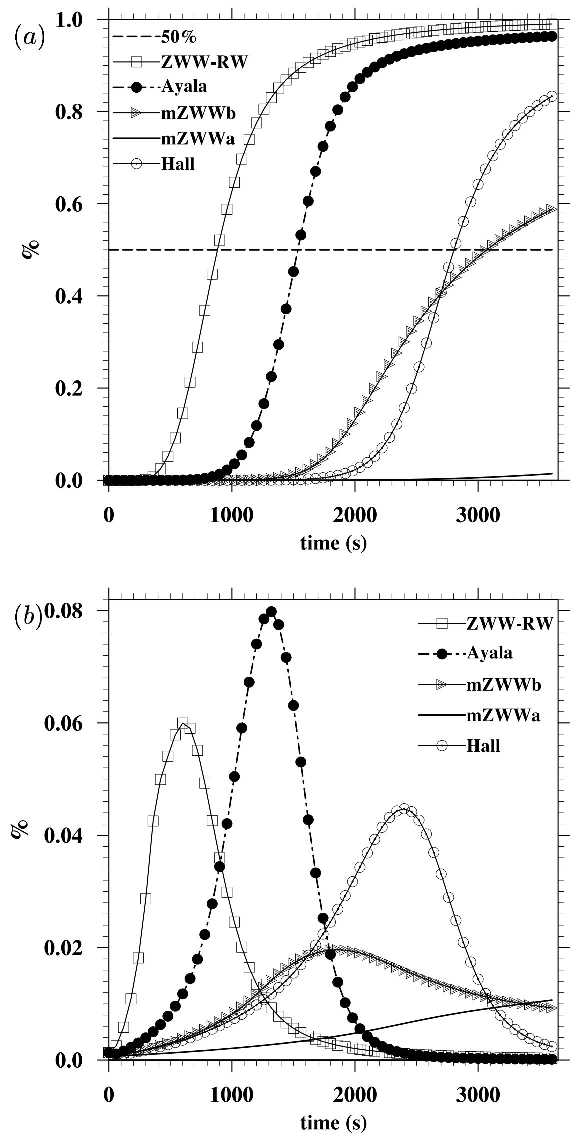

Figure 17: (a) The percentage of mass in droplets with radii greater than 50 μm. (b) The percentage of mass in droplets with radii from 20 μm to 100 μm.

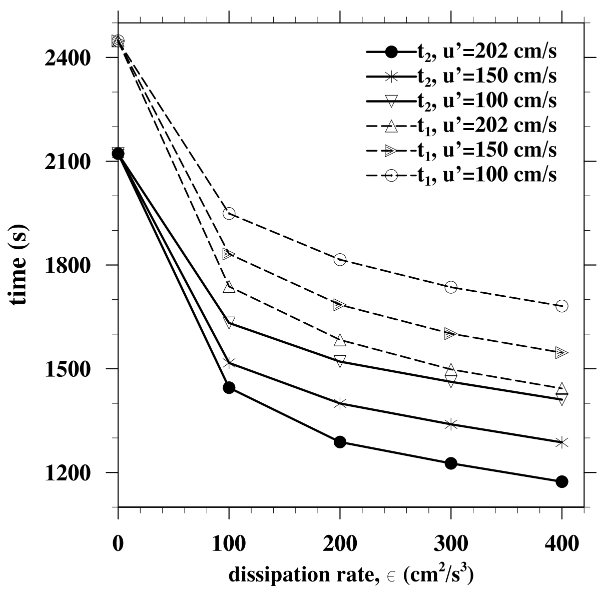

Figure 18: Characteristic times t_1 and t_2 under different turbulent dissipation rate and fluctuation velocity combinations.